Received: 4 March 2019 | Revised: 10 May 2019 | Accepted: 10 May 2019

DOI: 10.1002/sia.6663

RESEARCH ARTICLE

WILEY SURFACE and INTERFACE ANALYSIS

Nano-bio interface study between Fe content TiO_2 nanoparticles and adenosine triphosphate biomolecules

Tejal Barkhade[1] | Ambadas Phatangare[2] | Shailendra Dahiwale[2] | Santosh Kumar Mahapatra[3] | Indrani Banerjee[1]

[1] School of Nanosciences, Central University of Gujarat, Gandhinagar 382030, Gujarat, India

[2] Department of Physics, Savitribai Phule Pune University, Pune 411007, Maharashtra, India

[3] Department of Physics, Central University of Punjab, Bathinda 151001, Punjab, India

Correspondence
Indrani Banerjee, School of Nanosciences, Central University of Gujarat, Gandhinagar 382030, Gujarat, India.
Email: indrani.banerjee@cug.ac.in

Funding information
University Grants Commission

The advent of nano-biotechnology has inspired the interface interaction study between engineered nanoparticles (NPs) and biomolecules. The interaction between Fe content titanium dioxide (TiO_2) NPs and adenosine triphosphate (ATP) biomolecules has been envisioned. The effect of Fe content in TiO_2 matrix was studied using X-ray diffraction (XRD) and transmission electron microscopy (TEM). The increase in Fe content caused a decrease in particle size with change in morphology from spherical to one-dimensional rod structure. The Fe incorporation in the TiO_2 matrix reduced the transition temperature from anatase to rutile (A-R) phase along with formation of haematite phase of iron oxide at 400°C. The interaction of Fe content TiO_2 NPs with ATP molecule has been studied using spectroscopic method of Raman scattering and infrared vibration spectrum along with TEM. Fe content in TiO_2 has enhanced the interaction efficiency of the NPs with ATP biomolecules. Raman spectroscopy confirms that the NPs interact strongly with nitrogen (N_7) site in the adenine ring of ATP biomolecule. Engineering of Fe content TiO_2 NP could successfully tune the coordination between metal oxide NPs with biomolecules, which could help in designing devices for biomedical applications.

KEYWORDS

ATP biomolecule, Fe content TiO_2, interaction, Raman spectroscopy, α-Fe_2O_3

1 | INTRODUCTION

The growing field of nanotechnology in the context of interaction between nanomaterials and biomolecules creates a curiosity of investigation in the past few years. The interfaces involve physiochemical interactions, kinetics, and thermodynamic relations.[1-4] The nanoparticles' (NPs') features like size, shape, structure, porosity, and surface crystallinity determine the interaction kinematic.[1,5,6] The contact region with organic molecules, the solid-liquid interface, and the surface of NPs are important factors that are essential for nano-bio interface interactions.[6] Adenosine triphosphate (ATP) is currency of energy, whose production process occurs inside the inner mitochondrial membrane. Upon entry into cells, a variety of biomolecules may adsorb to the NP surface and reduce the NP surface energy by physical adsorption or chemical reactions.[7-10] NPs undergo certain interactions with the exposed cells and hence can affect mitochondria and so the ATP through binding with the biomolecules. Therefore, understanding the interactions of widely used nanoparticles ATP is of particular scientific interest. TiO_2 has found wide publicity as commercial products in our daily lives. TiO_2 NPs are widely used as food additives, drug delivery agents in personal care products, pharmaceuticals, papers, textiles, toothpaste, paints, plastics, and cosmetics.[11-14] Extensive applications of TiO_2 NPs have made the research of interface interaction with biomolecules of utmost importance. TiO_2 NPs have been found to be toxic depending on dosage, size, crystallographic phase, etc.[15,16] Devoid of its toxic effect, TiO_2 NPs have found immense usage in biomedical applications, which need to be addressed.[17] Therefore, material engineering to control the toxicity

for TiO_2 NPs has now been initiated. To minimize its toxic effect, transition metal ion like Fe has been used inside TiO_2 matrix. Fe^{3+} ions have been considered a suitable candidate, owing to the ionic radius of 0.64 Å being similar to that of Ti^{4+} (0.68 Å). Iron is a compound approved by the Food and Drug Administration, and it helps to slow the rate of parent particle dissolution and changes the particle matrix.[18] Incorporating Fe is a possible safe design strategy for preventing parent TiO_2 NPs toxicity and stability in animal cells and the environment.[19-21]

Moreover, TiO_2 and Fe content TiO_2 are strongly Raman active and, hence, could be explicitly studied to understand the interactions between these materials with ATP biomolecule. Vibrational spectra can give broad knowledge with respect to the molecular conformation and can be obtained by Raman spectroscopy. The Raman studies of the binding of divalent metal ions with the triphosphate moiety of ATP were reported by Rimai et al.[22,23] Zhelyaskov and Yue have shown that iron(III) has the ability to bind to ATP and adenosine monophosphate (AMP) by studying Raman spectral lines.[24] Bhaumik et al also reported the interaction study of ZnO with ATP biomolecules by using Raman spectroscopy.[25] The paper concentrates on the engineering of widely used TiO_2 NPs' size, shape, and morphology by Fe incorporation.

The present study made efforts to examine the reaction at the interface between ATP and Fe content TiO_2 NPs at all possible moieties in ATP using vibrational spectroscopy and transmission microscopy.

2 | EXPERIMENTAL DETAILS

Tetraisopropyl orthotitanate (TTIP), ethanol (C_2H_6O), anhydrous ferric chloride ($FeCl_3$), hydrochloric acid (HCl), ATP disodium salt (ATP-Na_2), and other chemicals were purchased from Sigma, SRL, and Merck, India. Deionized (DI) water was used throughout the reactions. All glassware was washed with dilute nitric acid (HNO_3) and distilled water and then dried in hot air oven.

2.1 | Synthesis of pure TiO_2 and Fe content TiO_2

The pure TiO_2 and iron content TiO_2 powder samples with different concentrations of Fe^{3+} were prepared through conventional sol-gel method.[26] In typical synthesis process, weight of $FeCl_3$ taken was 0, 0.32, 1.62, and 3.24 g in 20 mL of ethanol to prepare 0, 0.1, 0.5, and 1.0 mol%, respectively. Another solution of 4 mL of TTIP was dissolved in 20 mL of ethanol, on continuous stirring for 1 hour, in which 1 mL of HCl was added to form clear transparent solution. A different molar solution of $FeCl_3$ as prepared was added batchwise to each of TTIP clear transparent solution and was kept stirred for 2 hours at room temperature. In this way, pure TiO_2 and Fe content TiO_2 samples with different concentrations of Fe were prepared and named S_0, S_1, S_2, and S_3. The pH of about 2.0 was maintained during all the steps of synthesis process. Finally, distilled water was slowly added to the solution by stirring for 1 hour. The solution was dried at 80°C and calcined at 400°C for 2 hours. The synthesized powder was finally grounded and submitted for characterization.

2.2 | Sample preparation for interaction studies of ATP with TiO_2 and Fe content TiO_2

Two milligrams each of S_0, S_1, S_2, and S_3 samples was mixed separately into 200 μL of DI HPLC water, and 6 mg of ATP was mixed into 100 μL of DI water to form their respective solutions. The solutions were sonicated for 1 hour for uniform distribution. Two hundred microlitres of S_0, S_1, S_2, and S_3 NP solutions was mixed with 100 μL ATP solution and kept for sonication for 0.5 hours. The samples were stored at room temperature for 1 day. The samples were further sonicated for 10 min in DI HPLC water. The ATP biomolecules loosely bound to the NPs tend to detach themselves during the sonication process. We were mainly intending to study the Raman spectroscopy of the ATP biomolecules attached onto the surface of TiO_2 and Fe content TiO_2 nanostructures. The solid products were precipitated out and dried in air for further study of NPs and ATP interaction.[25]

2.3 | Characterizations of TiO_2 and Fe content TiO_2 NPs

The crystal structure of prepared samples was studied by powder X-ray diffraction (XRD) with a PANalytical Model X'Pert PRO diffractometer. The morphology, shape, size, and surface characteristics of the NPs were determined from transmission electron microscopy (TEM). The Fourier transform infrared (FTIR) (PerkinElmer Spectrum 65) spectra of the samples, in the range of 400 to 4000 cm^{-1}, were recorded as the percentage of transmittance (%*T*) versus wavenumber using KBr pellets. The FTIR spectrum was used to determine the chemical bonding and the interactions of NPs with the surface of the ATP molecules. The optical measurements were carried by using UV-Vis spectrophotometer (V-760 JASCO) in the mode of diffuse reflectance spectra (DRS) in the wavelength range of 200 to 800 nm. The powder samples were directly placed onto a cylindrical sample port holder (3-cm diameter, 1-mm depth). The photometric mode, %R, was selected before analysis. The Raman spectra of synthesized NPs (S_0, S_1, S_2, and S_3) were recorded on a Renishaw *inVia* laser Raman microscope equipped with wavelength of 533nm excitation source and spectra recorded for interaction with ATP samples with 633-nm excitation source. About 5 to 10 mW of laser power was used for recording the Raman spectrum of each sample for a period of 10 seconds.

3 | RESULTS AND DISCUSSION

3.1 | XRD analysis of synthesized samples

Figure 1 shows the XRD spectrum for all the synthesized NP samples calcined at 400°C for 2 hours. The figures corresponding to S_0 and S_1 show reflection from (101), (004), (200), (105), (211), (204), (116), (220), and (215) planes of anatase phase of TiO_2 without any traces

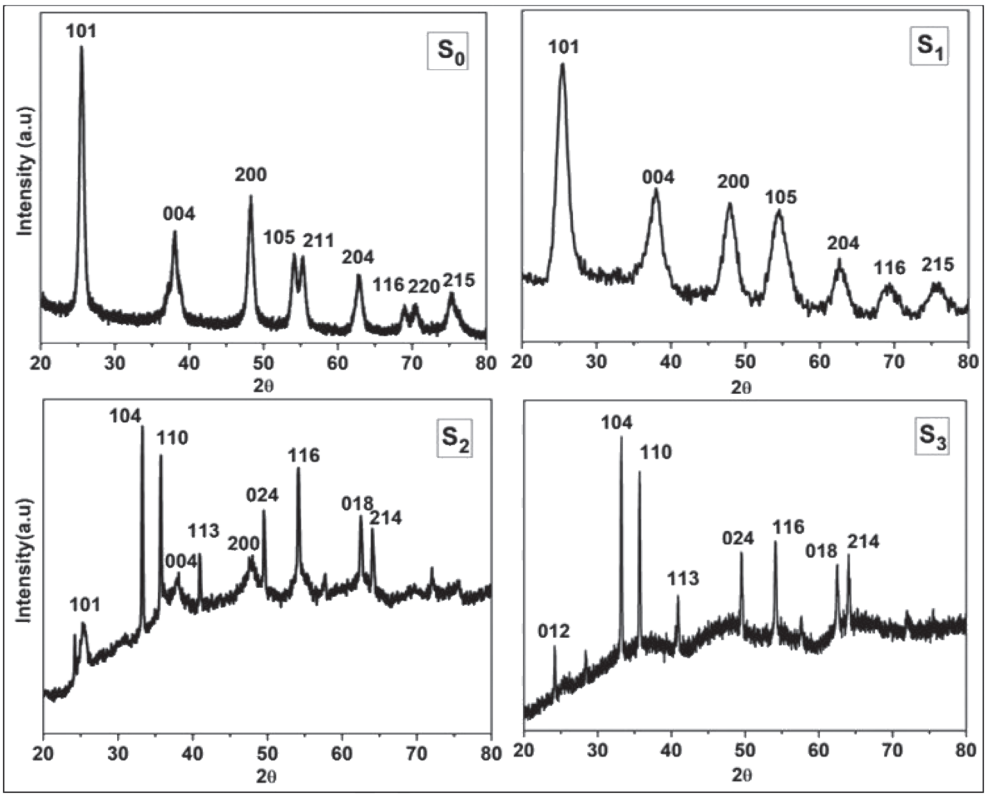

FIGURE 1 X-ray diffraction spectra of synthesized nanoparticles

of iron species. With the Pauling electronegativity and ionic radius of Fe^{3+} ion (1.83 and 0.064 nm) being similar to those of Ti^{4+} ion (1.54 and 0.068 nm), Fe^{3+} ions most likely reside in substitutional positions of TiO_2 crystal matrix forming solid solution in S_1 samples. The XRD spectrum representing sample S_2 shows decrease in the diffraction peak intensity from (101), (004), (200), (105), (211), (204), (116), (220), and (215) planes of anatase phase of TiO_2 and origin of a weakly intense reflection from (121) plane of rutile phase of TiO_2. The spectrum shows the presence of a shoulder peak attributed to (012) plane of α-Fe_2O_3 along with major peaks representing (104), (110), (113), (024), and (116) planes of most stable haematite phase of α-Fe_2O_3 (JCPDS card no. 33-0664) getting originated.

Sample S_3 shows almost complete transformation of anatase to rutile (A-R) phase along with formation of α-Fe_2O_3 as seen from the XRD spectrum. Because of increase of Fe concentration as in S_2 and S_3, the saturation limit of the substitutional Fe^{3+} is reached. Therefore, the redundant Fe^{3+} ions form α-Fe_2O_3 as follows[27]:

$$3O^{2+} + 2Fe^{3+} \rightarrow Fe_2O_3.$$

The present work shows the effect of Fe content on the phase transformation at a particular calcination temperature of 400°C. Although the A-R phase transformation temperature is reported to be above 600°C, S_1, S_2, and S_3 show A-R transformation at 400°C due to Fe incorporation. The Fe incorporation mechanism causes the Fe^{3+} ions to reside at the substitutional sites of parent TiO_2 matrix initially at a lower concentration. This causes oxygen vacancies due to charge compensation, and their movement drives the nucleation of rutile phase into existing anatase phase. The oxygen vacancies reduce the energy required to get overcome before the Ti–O octahedral rearranges, causing the phase transition to occur even at a lower temperature. Lowering of A-R transformation temperature for certain amount of Fe concentration is attributed to the thermodynamically driven kinetics. Anatase to rutile transformation is a metastable to stable phase transformation, without any phase equilibrium acquired during the process. Therefore, there is no definite temperature assigned for the transformation. The present paper shows that A-R transition occurs at 400°C with Fe incorporation in parent anatase TiO_2 phase matrix. The Gibb free energy for both the phases of parent TiO_2 material is given by[28]

$$G_{\text{anatase}}(\text{J/mol}) = -966\,798.3 + 463.4075T + \frac{0.854 \times 10^6}{T} + 0.312 \times 10^{-6}T^3 + 0.763\sqrt{T} - 75.323T\ln T + 1.124 \times 10^{-3}T^2,$$

$$G_{\text{rutile}}(\text{J/mol}) = -969\,145.6 + 462.5506T + \frac{0.011 \times 10^6}{T} + 0.202 \times 10^{-6}T^3 - 304.762\sqrt{T} - 73.799T\ln T - 3.014 \times 10^{-3}T^2.$$

The change in the Gibb free energy ΔG at 400°C is −1892.94 J/mol, which acts as the driving force for A-R transformation in the present work, whereas in S_2 and S_3 samples, formation of haematite phase

of Fe_2O_3 has also been possible. The full width at half-maximum (FWHM) (β) and the residual strain ε for the samples are related according to the following equation:

$$\beta \cos\theta = \frac{0.9\,\lambda}{D} + 4\,\varepsilon\,\sin\theta,$$

where D is the crystallite grain size and λ = 1.54 A. The plot of $\beta\cos\theta$ versus $\sin\theta$ gives a straight line.[29] The lattice strain due to Fe incorporation is calculated from the slope value. The lattice strain (ε) was calculated as 0.64×10^{-3}, 0.65×10^{-3}, 1.18×10^{-3}, and 0.21×10^{-3} for S_0, S_1, S_2, and S_3, respectively. The Fe incorporation causes increase in induced lattice strain for S_1 and S_2, whereas for S_3, the induced lattice strain gets redefined because of A-R transition accompanied with formation of completely new materials for phase of iron oxide. The increase in induced lattice strain for S_1 and S_2 samples indicates that Fe incorporation is accompanied with Fe substitution at some of the lattice sites of TiO_2 matrix forming iron titanium solid solution in these samples, whereas for S_3, phase transition and reformation of crystal structure occur as discussed above.

3.2 | TEM analysis of synthesized samples

The A-R phase transition and the change in structural morphology with increase in Fe concentration in TiO_2 have been studied using high-resolution TEM (HR-TEM) as shown in Figure 2. The S_0 (only TiO_2) and S_1 samples with low Fe content showed well-defined spherical particles of size 2.1 nm. The TEM analysis of the samples showed transformation from nanospheres to nanorods with incorporation of Fe in TiO_2 crystal. The anatase phase of the pure TiO_2 sample has been confirmed from selected area electron diffraction (SAED) pattern. The *d*-spacing was indexed with JCPDS data card no. 21-1272 of anatase phase, which was in agreement with the XRD analysis. The S_2 and S_3 samples with increasing Fe content showed transformation in the morphology from uniform spherical shape to elongated one-dimensional rod-like structure coexisting with the spherical NPs. Along with the morphological changes, the SAED pattern of the samples indicated the recrystallization from anatase phase to partial rutile and then formation of α-Fe_2O_3 in agreement with the XRD analysis.

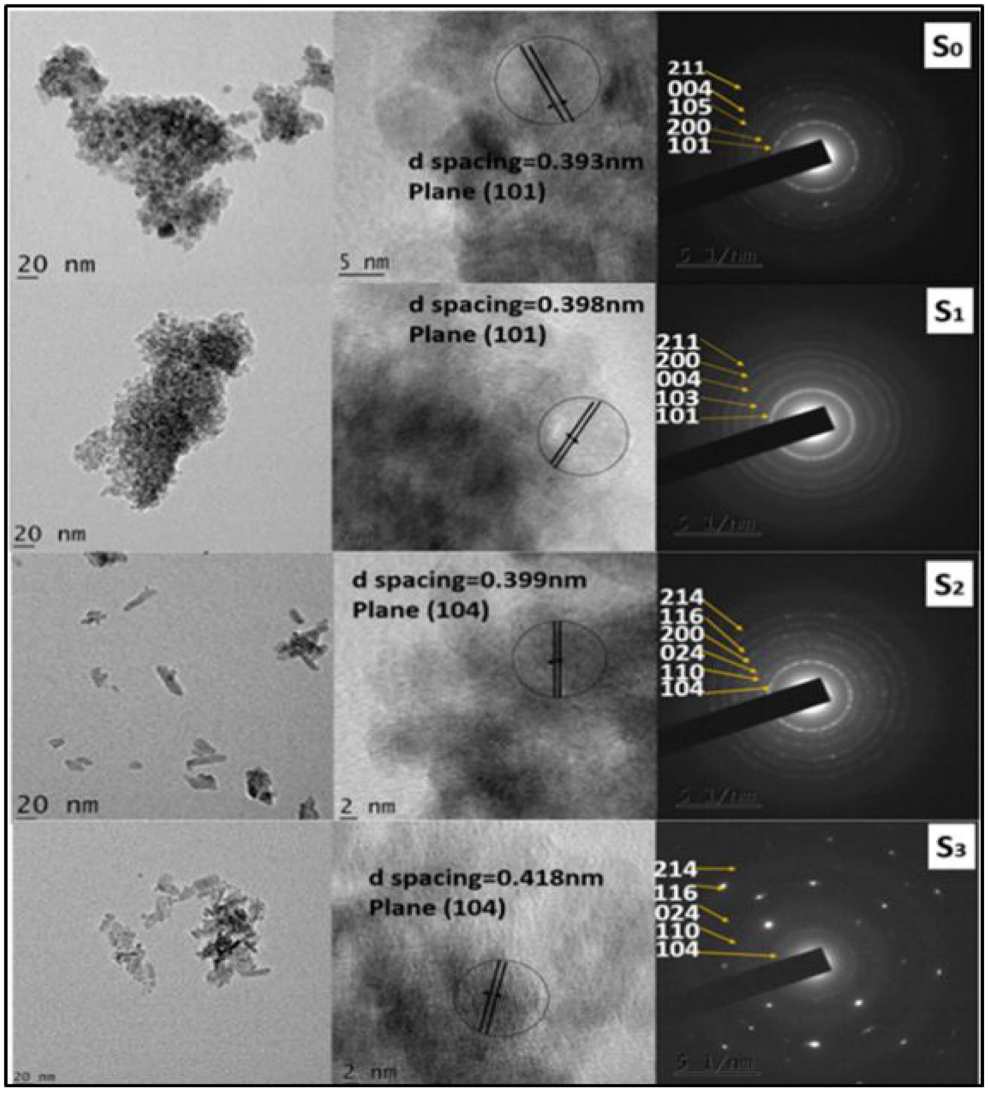

FIGURE 2 Transmission electron micrograph of synthesized nanoparticles with corresponding selected area electron diffraction patterns [Colour figure can be viewed at wileyonlinelibrary.com]

The *d*-spacing obtained from the SAED pattern was indexed with JCPDS card nos 21-1272, 21-1276, and 33-0664 corresponding to anatase TiO_2, rutile TiO_2, and α-Fe_2O_3. The HR-TEMs confirmed the increase in *d*-spacing as 0.393, 0.398, 0.399, and 0.418 nm for S_0, S_1, S_2, and S_3, respectively, with increase in Fe content. The distinguishable lattice spacing seen in the TEM has been indicated with their corresponding {*h*, *k*, *l*} planes.

Interestingly, TEMs of S_2 and S_3 samples showed elongated morphology with pointed edges. The nanoplates of α-Fe_2O_3 have been extensively reported to be bound by {102} plane. The crystals are generally crystallized in cubic and rhombic shapes having a diagonal growth direction along {104}. The pointed edges observed in S_2 and S_3 samples are of similar pattern as reported earlier. The aspect ratio (length/diameter) of the samples is found to increase from 12 for S_2 and 18 for S_3 sample.

3.3 | Raman spectra of synthesized NPs

The Raman bands observed for the samples have been presented in Figure 3A. The Raman spectrum supports the XRD data along with TEM analysis indicating the A-R transformation along with the formation of α-Fe_2O_3. The spectrum also explains the morphological changes from NPs to elongated structure due to Fe incorporation in the TiO_2 matrix. S_0 sample seems to possess the normal active modes of vibration corresponding to tetragonal anatase phase having A_{1g} + $2B_{1g}$ + $3E_g$ as predicted by the group theory.[29] The different vibrational modes correspond to E_g at 145 and 197 cm^{-1}, B_{1g} at 399 cm^{-1}, and (A_{1g} + B_{1g}) at 640 cm^{-1}. The S_1, S_2, and S_3 samples showed shifting in the Raman spectrum indicating the tendency of recrystallization from anatase to rutile (A-R transition) with increase in Fe concentration and also presence of bands corresponding to α-Fe_2O_3. The shifting of 144 to 145 cm^{-1} shows resemblance to rutile phase formation as supported by XRD data, which further get shifted to higher values because of gradual increase of Fe content in the matrix. The difference in the shift of E_g mode is due to the change in Ti–O bond on account of Fe inclusion. The Raman band at 232 cm^{-1} in S_2 and S_3 is attributed to the infrared active (Raman active) doubly degenerate E_u mode coinciding for both rutile and Fe_2O_3. The appearance of Raman inactive mode in violation of selection rule is due to the change in effective mass (μ) at the Ti sites due to Fe, which is given as

$$f = \frac{1}{2\pi}\sqrt{\frac{k}{\mu}}, \text{ where } \mu = \frac{m_1 m_2}{m_1 + m_2},$$

k is the molecular force constant and μ is the reduced mass. The occurrence of 297 cm^{-1} resembles the Raman mode of Fe_2O_3. According to group theory, α-Fe_2O_3 possesses seven Raman active vibration modes: two A_{1g} and five E_g. The bands appearing at 232 and 498 cm^{-1} represent A_{1g} modes, whereas 242, 293, 412, and 613 cm^{-1} resemble the E_g mode in S_2 and S_3 samples only. Literature reveals that E_g and A_{1g} modes of vibrations are orientation dependent. In the zz configuration, A_{1g} modes are allowed, whereas in the crossed xz and yz polarization, only the E_g modes are allowed with less intensity of A_{1g}. The allowed vibration of A_{1g} along one direction clearly explains the phonon confinement along one direction.[30]

The elongated morphology of the particles as observed from TEM is therefore justified from the observed active vibrations in S_2 and S_3 samples. The intense peak observed in S_2 and S_3 samples at 1310 cm^{-1} also gives insights of the formation of α-Fe_2O_3. The lateral optical (LO) mode at 655 cm^{-1} is Raman forbidden, and only the broad 2LO band is observed, and it is also with enhanced intensity due to the resonance enhancement. The phonon line is attributed to the two magnon scattering arising from the interaction of two magnons

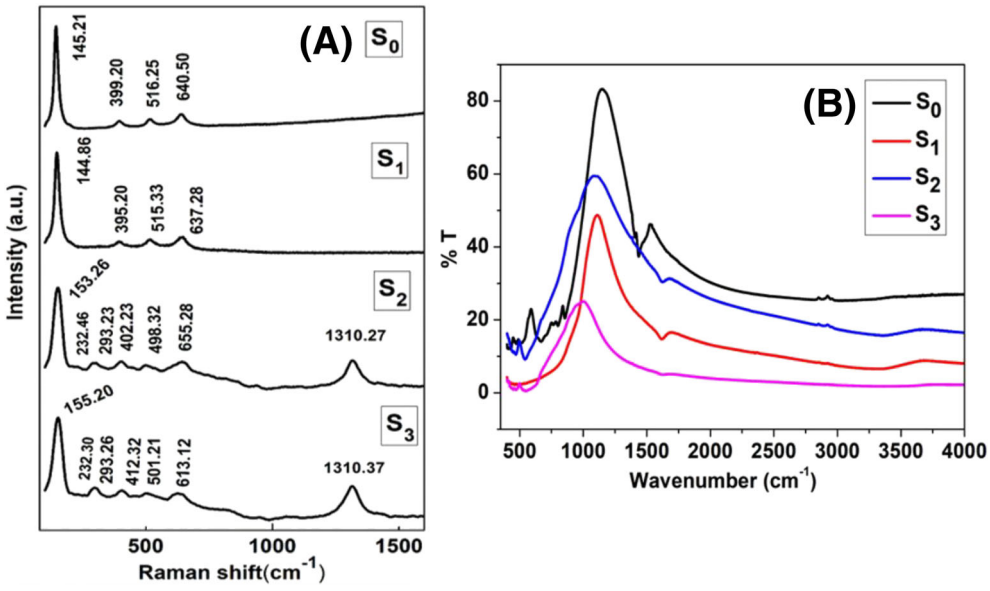

FIGURE 3 (A) Raman and (B) Fourier transform infrared spectra of synthesized nanoparticles

created on antiparallel close spin sites. The Raman spectrum of semiconductors gets red shifted and broadened because of the relaxation of q vector selection rule. According to the Heisenberg uncertainty principle, the fundamental $q \approx 0$ Raman selection rule is relaxed for a restricted size domain. The phonon wave vector uncertainty goes approximately as $\Delta q \approx 1/D$, where D is the crystal diameter.[30-32] The spatial confinement of the optical phonon gets decided by the size and shape of the NPs. With increase in grain size, the Raman bands become stronger and sharper with a red shift towards a lower wavenumber. The corresponding shift in the band positions is due to the Fe incorporation, which induce changes in structure, defects, or particle sizes.

3.4 | FTIR of synthesized NPs

The vibrational spectra of the samples in Figure 3B suggest that the chemisorption of molecules and ions on crystal surface can modify the growth direction/morphology due to surface energy. The FTIR detects the presence of surface elements revealing the morphological evolutions due to the vibration modes along or perpendicular to one specific direction of lattice. The unidirectional growth could be explained from the FTIR spectra as like that of Raman spectra, as explained in the preceding section. The metal oxide peaks are mostly detected between 400 and 800 cm^{-1}. The S_0 sample showed vibration mode at 510 to 653 cm^{-1} for Ti–O and 740 cm^{-1} resembling the Ti–O stretching mode for Ti–O–Ti as in the case of pure TiO_2. The vibration bands show shift and occurrence of new bands resembling that of haematite phase of iron oxide for the spectra representing S_1, S_2, and S_3 samples with increased Fe content. Group theoretical analysis predicts that haematite possesses six infrared active modes: two polarized along the c-axis (|| mode) and the four perpendicular to the c-axis ($\perp$ mode).[33] The absorptions at 440 and 522 cm^{-1} exhibit $\perp$ modes, and 650 cm^{-1} exhibits || mode, which gets generated in S_1, S_2, and S_3 samples because of Fe content. The spectra for S_1, S_2, and S_3 also showed an IR active band at 1622 cm^{-1} resembling the vibration mode for Ti–O–Fe stretching, which increases the surface hydroxylation with Fe content. Therefore, the IR absorbance spectra clearly indicated the mixed phase formation in the crystal.

Moreover, literature reveals that infrared optical vibrations are morphology dependent as the induced polarization changes because of external electromagnetic field on the crystal lattice. The spectra between 400 and 700 cm^{-1} clearly indicate that the absorbance peak of 510 and 650 cm^{-1} in S_0 gets merged with characteristic absorptions of $\perp$ modes at 440 and 522 cm^{-1} and || mode at 650 cm^{-1} of haematite in Fe content samples of S_1, S_2, and S_3. The band at 1622 cm^{-1} is seen in all Fe content TiO_2 samples, which represent molecular stretching of Ti–O–Fe.[26] This band signifies that there is a higher percentage of absorbance in the infrared region, which causes the increase in surface hydroxylation with incorporation of Fe into TiO_2. It also confirms the formation of Ti–O–Fe bond functional group.

3.5 | DRS of synthesized NPs

Like vibrational spectra, the electronic spectra of the samples also provide shape- and morphology-dependent information. The electronic spectra of the synthesized samples were characterized using DRS. Figure 4A shows the reflectivity (R%) versus wavelength graphs of all the prepared samples. The reflectance decreases with increase in Fe content. The optical band gap of all the samples was determined from DRS spectra. Sample S_0 (without Fe content) showed wide absorbance in the UV region, with high reflectance beyond 350 nm having optical band gap of 3.4 eV. The wide absorbance between 200 and 350 nm is related to the ligand-to-metal charge transfer transitions. The reflectance gradually decreases with increase in Fe content with shift in absorption band edge towards higher wavelength.

The spectra for S_2 and S_3 samples expressed the biggest shift in the value of λ_{max} reaching 448 nm and the value of optical band gap of E_g decreasing to 2.50 eV as Fe concentration is increased. Figure 4B shows the change in optical band gap E_g with increase in Fe concentration for the samples. The features observed for S_2 and S_3 samples showed the presence of multiple humps signifying absorbance related to Fe^{3+} ligand field transitions as $^6A_1{}^4T_1$ (^4P) at 290 to 310 nm, and $^6A_1{}^4E$ (^4D) and $^6A_1{}^4T_2$ (^4D) at 360 to 380 nm for α-Fe_2O_3 phase, respectively. The observed hump at 485 to 550 nm is

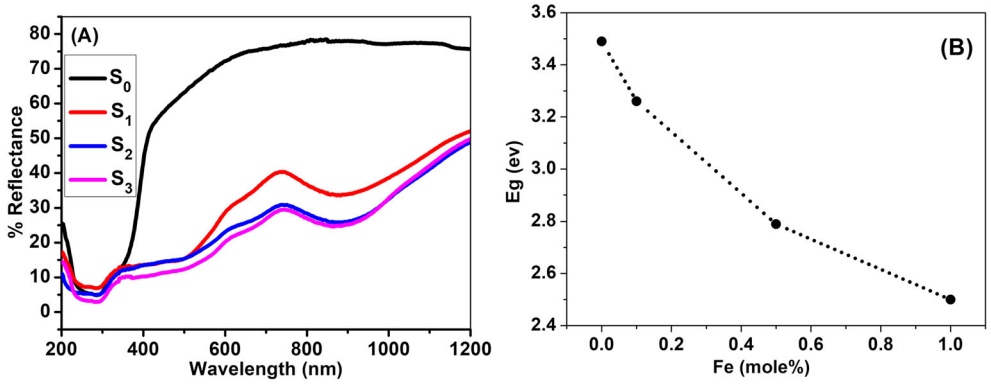

FIGURE 4 A, Diffuse reflectance spectra of synthesized nanoparticles. B, Variation of energy band gap with increasing Fe content

related to the pair excitation processes of $^6A_1 + {}^6A_1\ {}^4T_1\ (^4G) + {}^4T_1\ (^4G)$ at 485 to 550 nm. This probably arise because of the overlapped contributions of $^6A_1{}^4E$ and $^4A_1\ (^4G)$ ligand field transitions at 430 nm and the charge transfer band tail. The third band transition at the range of 580 to 700 nm is assigned to the $^6A_1\ {}^4T_1\ (^4G)$ at 620 nm in the red range arising because of the spin-forbidden ligand field transitions, and the last band transition at 700 to 900 nm is attributed to another $^6A_1\ {}^4T_1\ (^4G)$ at about 785 nm in the infrared region, which also contributed to ligand field transitions of Fe^{3+}. In accordance to the selection rules, the charge transfer transitions or the pair transitions are much stronger than those from field transitions.[34]

3.6 | Raman spectra of pure and hydrolysed ATP

Figure 5A represents the Raman spectra of pure ATP along with the moieties present in the energy biomolecule. The first Raman studies of the binding of divalent metal entities with the triphosphate moiety of ATP were reported by Rimai et al. The Raman spectra of pure ATP consist of three distinct sets of peaks: one characteristic of adenine ring vibrations, which is depicted in blue-coloured wavenumbers, the other characteristic of the triphosphate modes in pink-coloured wavenumbers, and another at 524.3 cm^{-1} of peak for ribose moiety is shown in green-coloured wavenumber in the graph

In pure ATP, ring vibrations of the adenine moiety at 312.5, 699.0, 721.5, 1275.1, 1316.5, 1493.6, and 1548.5 cm^{-1} were observed. For phosphate moiety, vibrations at 810.0, 899.9, and 1117.2 cm^{-1} and for ribose moiety vibrations at 524.3 cm^{-1} were observed. Thus, specific interactions of triphosphate and adenine moieties can be monitored simultaneously. In this study, we focus our attention on the interaction of TiO_2 and Fe content TiO_2 nanostructures (S_0, S_1, S_2, and S_3) with the different moieties of ATP at neutral solution. Raman scattering techniques do not suffer any restriction and are capable of revealing different modes of binding between metal oxides and the adenine moiety in terms of direct coordination (eg, at N_1, N_7, or $-NH_2$) or charge transfer complex formation. The five probable nitrogen binding sites in the adenine entity are the pyrimidine N_1 and N_3 and imidazole N_7 and N_9 ring nitrogen and exocyclic $-NH_2$. The C=C bond can play an active role in binding too.[24] Reviewing the interaction of the adenine entity with divalent metal ions may illustrate a better understanding of the N donors in binding.

Figure 5B represents the Raman spectra of hydrolysed ATP. Suspension of ATP involves formation of hydrogen bonds with water molecules, and a significant Raman shift of the bond occurs, playing an active role in hydrogen bond formation. Upon hydrolysis, a greater shift in this bending mode occurs because of the formation of the hydrogen bond. The ribose ring in ATP occurs as a weak Raman active mode and is visible as smeared-out peaks in the range from 553.20 to 641.52 cm^{-1}. Hydrolysis of ATP introduces a change in the structural vibrational modes, and the adenine ring modes are mostly affected. All the vibrational frequencies ranging from 812.46 to 940.21 cm^{-1} represent phosphate stretching modes (O–P–O) present in the ATP

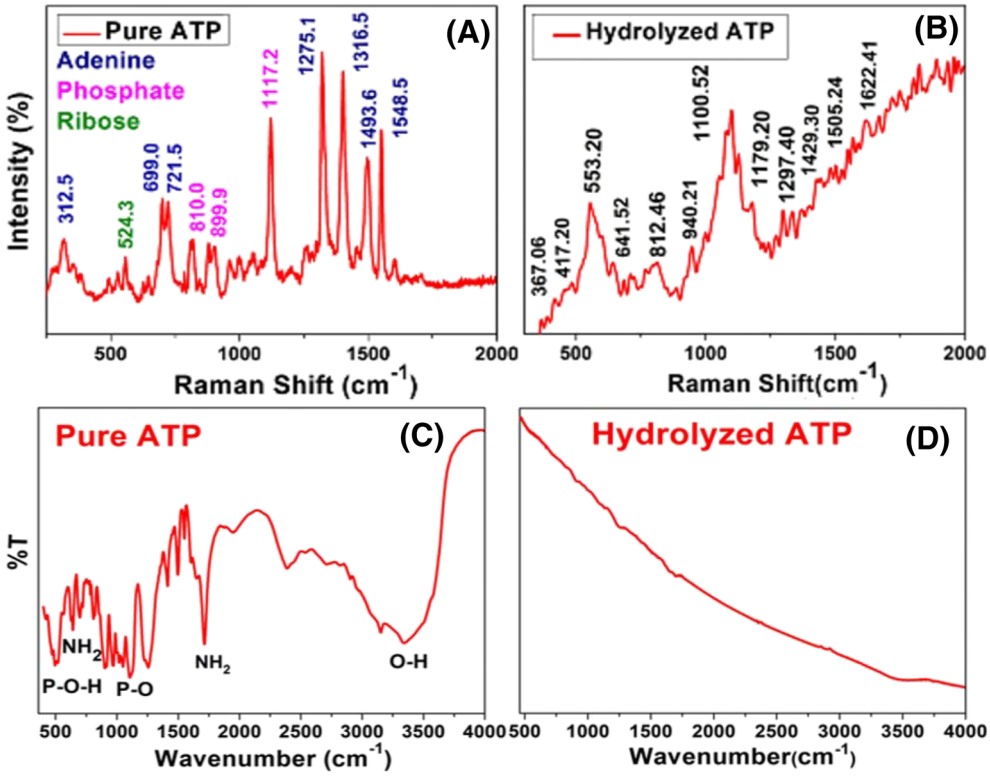

FIGURE 5 Raman spectra: (A) pure ATP; (B), hydrolysed ATP. Fourier transform infrared spectra: (C), pure ATP; (D), hydrolysed ATP. ATP, adenosine triphosphate

biomolecule.[35] Small changes in these vibrational modes indicate insurgency during the process of hydrolysis. The peak corresponding to wavenumber 1100.52 cm^{-1} indicates the two phosphate stretching vibrations in the ATP biomolecule. The adenine vibrations are the most prominent in the ATP molecule and form the backbone of vibrations ranging from 1100.52 to 1429.30 cm^{-1}. These vibrations of the adenine ring undergo shift in vibrational frequency due to the formation of hydrogen bonding at the NH_2 site.

The adenine bond involving the vibrations from N_1C_6–NH_2 at 312.5 cm^{-1} of pure ATP gets shifted to 367.06 cm^{-1} on hydrolysis. The ribose moiety has weak Raman scattering in than have other moieties in pure ATP spectrum, which gets enhanced, showing a sharp peak at 553.20 cm^{-1} on hydrolysis due the perturbation of other vibration modes associated with it. The sharp peaks at 699 cm^{-1} represent the out-of-plane waging of NH_2 bonds and at 721.1 cm^{-1} resemblance the adenine ring breathing mode, when all the bonds stretch coherently or might arise because of the vibrations from adenine perturbed ribose rings as $D.N_9R$ and N_1C_4 bonds, where R represents the ribose rings.[24,35] Hydrolysis causes structural deformation mostly affecting the adenine ring modes. The sharp peaks of 699 and 721.1 cm^{-1} merge into a broad less intense peak at 641.52 cm^{-1}. The hydrogen bond formed at the NH_2 site annihilates the out-of-plane wagging of vibrations in this entity.

Hydrolysis also affects the phosphate moieties having the stretching modes (O–P–O) at 810 and 901 cm^{-1} in pure ATP that gets merged and centred at 812 cm^{-1}. This stretching mode plays an important role in interaction kinetics with metal oxide NPs. Another distinct peak at 1117.2 cm^{-1} featuring two phosphate stretching vibrations in pure ATP molecule gets shifted to broad peak at 1100 cm^{-1} due to hydrolysis. The adenine vibrations ranging from 1000 to 1750 cm^{-1} consisting of 1275.1 cm^{-1} corresponding to stretching modes of C_8N_7, C_8N_9, and N_1C_2 bonds and bending modes of N_1C_2 and C_2H bonds are observed. The vibrational modes at 1316.8 cm^{-1} represent stretching vibrations of N_9C_8 and N_3C_2 and bending vibrations of C_8H and C_2H bonds. The other peaks observed at 1316.5 cm^{-1} correspond to vibrations from C_5N_7 and C_8N_9 bonds, 1493.6 cm^{-1} corresponds to stretching of C_4N_9 and bending of C_8H bond, and 1548.5 cm^{-1} corresponds to vibrations from N_3C_4 and C_4C_5 bonds in adenine moiety. The two distinct peaks of 1275.1 and 1316.5 cm^{-1} get merged into single peak positioned at 1297.40 cm^{-1} after hydrolysis. The occurrence of new peak at 1297.40 cm^{-1} with demolition of two distinct peaks predicts the physicochemical reaction of the ATP biomolecules to be active at the N_7 atomic site. The hydrolysis mechanism imparts changes in terms of shifting as well as intensity variation due to hydrogen bond formation at NH_2 site.[25]

3.7 | FTIR spectra of pure ATP and hydrolysed ATP

The FTIR spectra of pure ATP and hydrolysed ATP are depicted in Figure 5C,D. The spectrum in Figure 5C representing the pure ATP sample shows intense absorptions from the vibrations corresponding to different moieties of ATP. The broad band at 3341 cm^{-1} is attributed to the surface absorbed water in the samples. The vibrational bands at about 814, 1410, 1489, 1547, 1602, and 1713 cm^{-1} are assigned to adenine moiety. The bands arising in pure ATP sample at 504 and 703 cm^{-1} are assigned to the asymmetric and symmetric stretching vibrations of the triphosphate group, and those at 904 and 1108 cm^{-1} are assigned to the P–O bond originating from both adenosine groups.[36] The characteristic P–O–H band around 920 cm^{-1} confirms presence of phosphoryl group in pure ATP.

The FTIR spectrum in Figure 5D for the hydrolysed ATP shows less intense peaks. This might be due to multiple reasons of protonation state, conformation, and metal chelation of ATP occurring with water solvent during hydrolysis. Reported H-NMR experiments show that ATP molecule in water exists in a linear anticonfiguration, and the triphosphate tail gets fully protonated under neutral conditions.[37] The small band assigned to 990 cm^{-1} in the spectrum confirms the occurrence of protonation phenomenon, ie, addition of proton, H^+, to phosphate ion for the present sample. The bands at 1090 and 1124 cm^{-1} are assigned to protonated phosphate ions due to fluctuation of proton in hydrogen bond, also confirming the hydrolysis of ATP from FTIR spectra.[38]

3.8 | Nano-bio interface interaction study

All the synthesized samples were interacted with ATP. The present paper is an effort to understand the interaction of Fe content TiO_2 NPs/nanorods with ATP molecules. Both Raman and infrared spectroscopies are concerned with the vibrational spectra that give the comprehensive information about the molecular conformation.[39] However, IR spectra undergo strong absorption of water in the IR range, which sometimes limits its usage to understand certain interactions with biomolecules. The present work deals with both IR and Raman spectroscopic analyses to understand the interactions. Suspension of ATP involves formation of hydrogen bonds, which cause the shifts in the respective bonds representing the moieties of pure ATP.

Figure 6 shows the Raman spectrum for the interacted synthesized NPs with ATP biomolecules. The physicochemical interaction between the NPs and ATP molecules was allowed by keeping the mixture in suspension for 24 hours under room temperature condition. The comparative Raman spectra of the untreated and treated hydrolysed ATP molecules with NPs would reveal the interaction process. The TiO_2 NPs (sample S_0) seem to get attached with the ATP molecules for which the red shift and increased peak width for the adenine moiety at 241 and 323 cm^{-1} were observed. These sites correspond to both stretching and bending of $-NH_2$ bonds. Apart from adenine group, all other groups of moieties seem to get suppressed, and no vibrational modes were observed. The Fe content samples (S_2 and S_3) showed enhanced interactions. The occurrence of significantly intense lines between 750 and 1750 cm^{-1} reveals enhanced interactions of ATP due to Fe content in NPs. This might be because the bond coordination efficiency of Fe is more, which increases the probability of attachment with the active sites of ATP molecules.

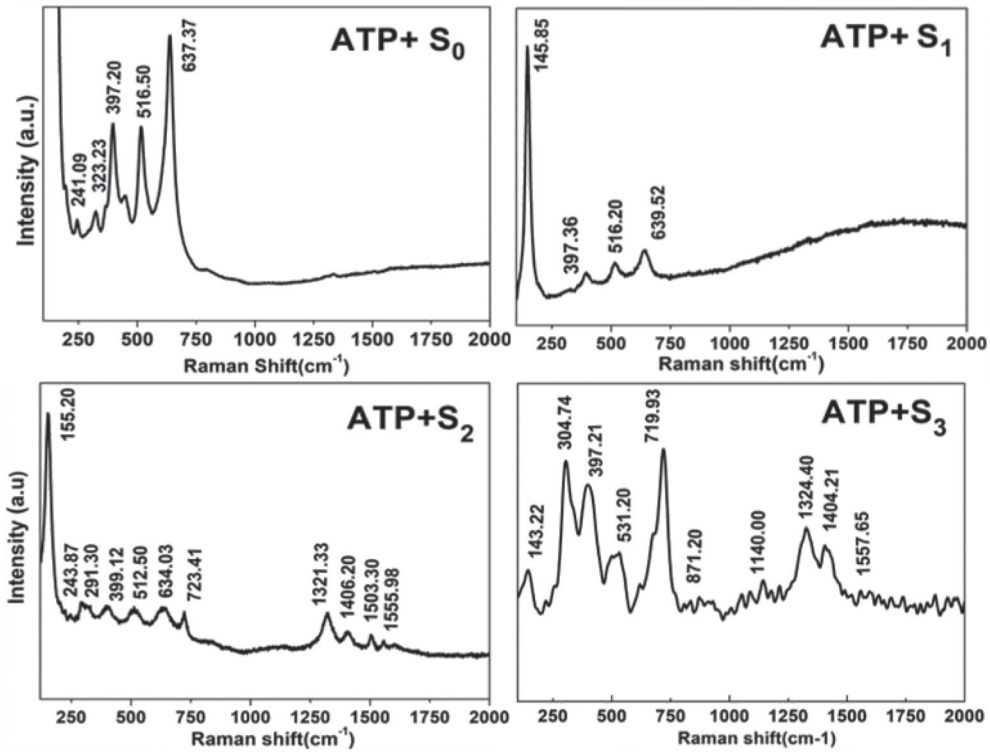

FIGURE 6 Raman spectra of samples interacting with ATP. ATP, adenosine triphosphate

Moreover, with increase in Fe content in S_2 and S_3, the one-dimensional morphology provides increased effective surface area for interaction. The distinct features of interaction at the adenine and the phosphate groups are observed. The broadening of the peaks corresponding to 291, 399, 512, and 634 cm^{-1} occurs because of the merging and superimposed vibrations occurring simultaneously from Fe_2O_3 molecules along with adenine, ribose, and phosphate groups of ATP molecules. The single peak of adenine at 723 cm^{-1} in the interacted samples also indicated interactions between NPs and adenine group of ATP molecules. The Fe content NPs caused a decrease in intensities of the vibration bands responsive to hydrolysed ATP at 812 and 1100 cm^{-1}. These bands correspond to the in phase and out of phase of symmetric PO_2^- and stretching vibrations of terminal phosphate group of ATP. Noticeable frequency shift of 812 and 1100 cm^{-1} of hydrolysed ATP to 871 and 1140 cm^{-1} and the broadening indicate direct involvement of the phosphate moiety in

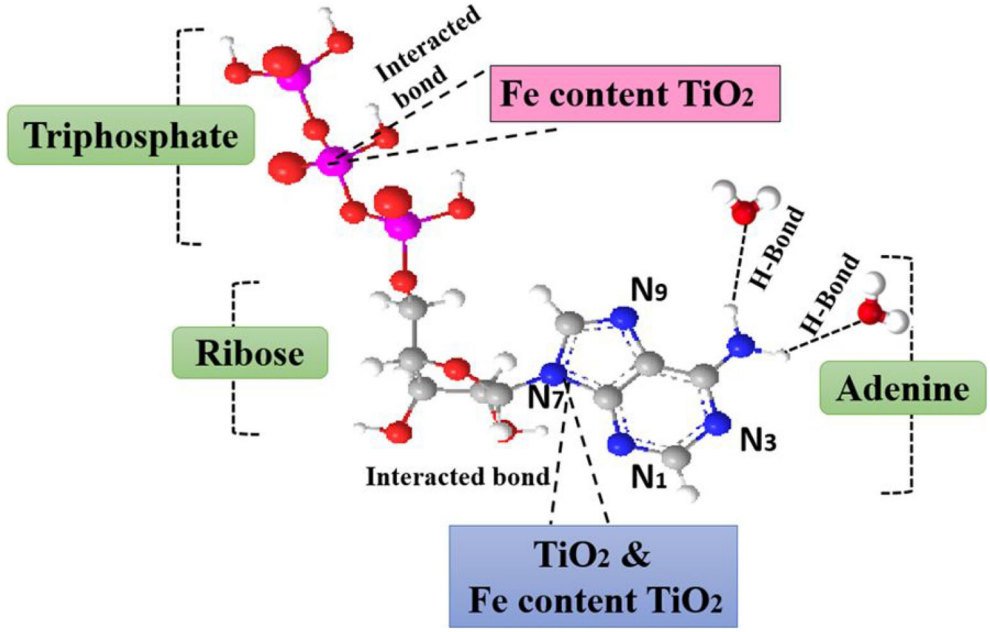

FIGURE 7 Schematic diagram of interaction model of Fe content TiO_2 nanostructures with adenosine triphosphate biomolecule

complexation with Fe^{3+} ions in S_2 and S_3 samples. A very distinct vibration at 1404 cm^{-1} was observed in S_2 and S_3 samples. The vibration at 1404 cm^{-1} corresponds to the N_7 site of adenine group. The generation of this new peak indicates formation of new bond with the ATP molecules that get instigated with Fe ions. Fe enhances the coordination of metal oxide NPs with the ATP biomolecules. The longer chain of phosphate moiety in ATP forms a closed structure of ATP-Fe complex when interacted with Fe content TiO_2 NPs. The interaction at N_7 nitrogen of adenine also seems to be favourable for interactions. The ATP-Fe complex has been reported to be of anticonformation.

The most active interaction sites are N_7 of the adenine moiety of ATP molecules. The observed red shift and peak broadening of 323 cm^{-1} involving the stretching and bending of $-NH_2$ bond also confirm the possible interaction. The observed spectral shift, broadening, and intensities are very small. This is because with the interaction medium being water, the direct coordination between the metal ions and N_7 is separated by water molecules as suggested by NMR analysis.[40] The relatively strong vibration mode occurring at 1404 and 1406 cm^{-1} for, respectively, S_2 and S_3 samples indicates the enhancement in the ability of coordination between NPs and ATP biomolecules. Interestingly, this band is missing for S_0 and S_1 samples.

Figure 7 shows the interaction model between Fe content TiO_2 NPs and ATP on the basis of Raman spectroscopy studies, and it clearly shows the binding site of ATP biomolecule with NPs. TiO_2 and Fe content TiO_2 strongly bind with N_7 atom in the adenine ring and also with the phosphate group of ATP biomolecule. The blue balls represent nitrogen (N), white balls represent hydrogen (H), red balls represent oxygen (O), and grey balls represent carbon (C).

The FTIR was obtained for supporting the Raman analysis to understand the attachment of ATP to the synthesized NPs' surface depicted in Figure 8. Characteristics of P–O band around 1108 cm^{-1} were found in pure ATP sample. However, the absence of the characteristics P–O–H band around 904 cm^{-1} in the ATP-NPs' interacted samples could suggest that the phosphoryl groups get deprotonated

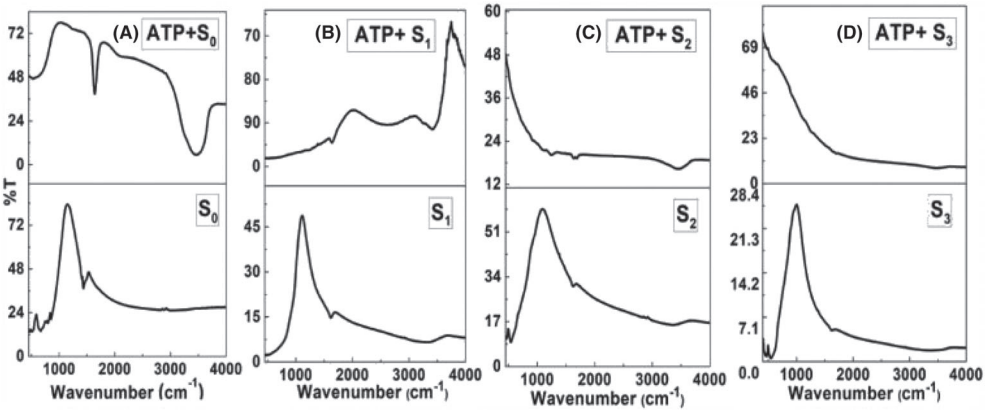

FIGURE 8 Fourier transform infrared spectra of interacting samples with ATP

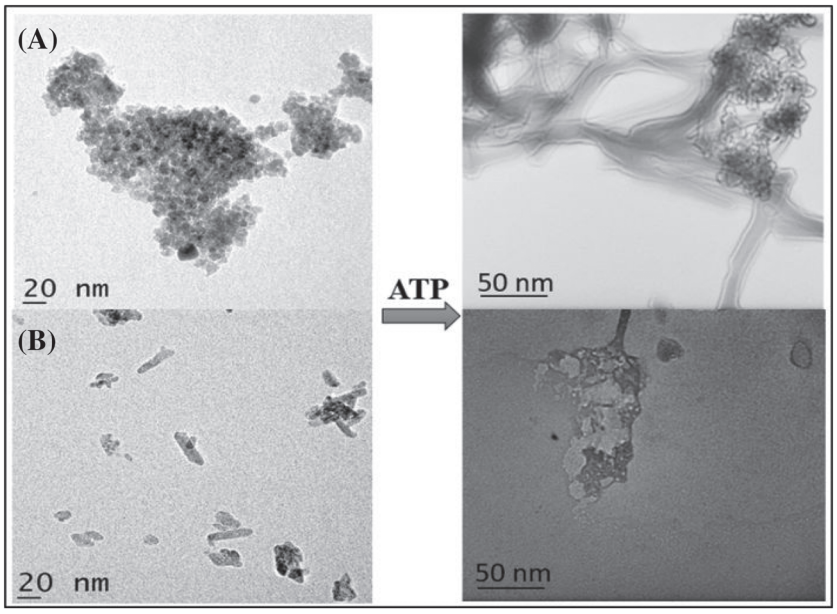

FIGURE 9 Transmission electron microscopy image of ATP interacted with (A) TiO_2 and (B) 0.5% Fe content TiO_2. ATP, adenosine triphosphate

after NP interaction. Moreover, FTIR spectroscopy also confirmed that ATP had been successfully grafted onto all the samples.[41]

Typical TEM images showing the spherical particles in S_0 and nanorods in S_3 interacted with ATP have been presented in Figure 9A,B. The ATP and NPs' interaction has been performed using a fast and simple aqueous method. The interface interaction of ATP with NPs is driven via adsorption process. The adsorption of oppositely charged ATP molecules on NP surface occurs without the need for any complex chemistry or the use of linkers. The ATP biomolecule adheres with the synthesized samples easily. Moreover, ATP has a good cation exchange capacity and thus can attract the NPs to its surface.[42]

4 | CONCLUSIONS

Fe enhances the physicochemical interaction of TiO_2 metal oxide NPs with ATP biomolecules. The amino group of adenine moiety, which acts as the backbone of ATP biomolecules, provides the most active sites for coordination, whereas terminal phosphate groups also prove to be potential interaction sites. Since the interaction medium is water suspension, the direct coordination of NPs to N_7 sites is expected to be separated by water molecules. A completely new coordination site attached to stretching of adenine group is triggered by Fe ions at 1404 cm^{-1}. It could be speculated that Fe content can instigate new coordination sites, increasing the physicochemical interactions between TiO_2 NPs with ATP biomolecules. Such tuning of coordination between metal oxide NPs with biomolecules could help in designing devices for biomedical applications.

ACKNOWLEDGEMENTS

The first author is grateful to University Grants Commission, New Delhi, for awarding the Rajiv Gandhi National Fellowship for financial support. The authors would like to express thanks to CIF, Central University of Gujarat, GFSU (IR&D), Gandhinagar, and Department of Physics, Savitribai Phule Pune University, Pune, for providing the characterization facilities for the samples.

CONFLICTS OF INTEREST

There are no conflicts to declare.

ORCID

Indrani Banerjee https://orcid.org/0000-0002-0230-7888

REFERENCES

1. Oberdörster G, Maynard A, Donaldson K, et al. Principles for characterizing the potential human health effects from exposure to nanomaterials: elements of a screening strategy. *Part Fibre Toxicol*. 2005;2(1):1.
2. Nel A, Xia T, Mädler L, Li N. Toxic potential of materials at the nanolevel. *Science*. 2006;311(5761):622-627.
3. Vertegel AA, Siegel RW, Dordick JS. Silica nanoparticle size influences the structure and enzymatic activity of adsorbed lysozyme. *Langmuir*. 2004;20(16):6800-6807.
4. He X, Aker WG, Fu PP, Hwang HM. Toxicity of engineered metal oxide nanomaterials mediated by nano-bio-eco-interactions: a review and perspective. *Environ Sci Nano*. 2015;2(6):564-582.
5. Velegol D. Assembling colloidal devices by controlling interparticle forces. *J Nanophotonics*. 2007;1(1):012502.
6. Nel AE, Mädler L, Velegol D, et al. Understanding biophysicochemical interactions at the nano-bio interface. *Nat Mater*. 2009;8(7):543-557.
7. Yue Y, Li X, Sigg L, et al. Interaction of silver nanoparticles with algae and fish cells: a side by side comparison. *J Nanobiotechnol*. 2017;15(1):16.
8. Lynch I, Dawson KA. Protein-nanoparticle interactions. *Nano Today*. 2008;3(1–2):40-47.
9. Monopoli MP, Walczyk D, Campbell A, et al. Physical-chemical aspects of protein corona: relevance to in vitro and in vivo biological impacts of nanoparticles. *J Am Chem Soc*. 2011;133(8):2525-2534.
10. Liu W, Rose J, Plantevin S, Auffan M, Bottero JY, Vidaud C. Protein corona formation for nanomaterials and proteins of a similar size: hard or soft corona. *Nanoscale*. 2013;5(4):1658-1668.
11. Martirosyan A, Schneider YJ. Engineered nanomaterials in food: implications for food safety and consumer health. *Int J Environ Res Public Health*. 2014;11(6):5720-5750.
12. Anselmann R. Nanoparticles and nanolayers in commercial applications. *J Nanopart Res*. 2001;3(4):329-336.
13. Weir A, Westerhoff P, Fabricius L, Hristovski K, Von Goetz N. Titanium dioxide nanoparticles in food and personal care products. *Environ Sci Technol*. 2012;46(4):2242-2250.
14. Jovanović B. Critical review of public health regulations of titanium dioxide, a human food additive. *Integr Environ Assess Manag*. 2015;11(1):10-20.
15. Trouiller B, Reliene R, Westbrook A, Solaimani P, Schiestl RH. Titanium dioxide nanoparticles induce DNA damage and genetic instability in vivo in mice. *Cancer Res*. 2009;69(22):8784-8789.
16. Chang X, Xie Y, Wu J, Tang M, Wang B. Toxicological characteristics of titanium dioxide nanoparticle in rats. *J Nanosci Nanotechnol*. 2015;15(2):1135-1142.
17. Yin ZF, Wu L, Yang HG, Su YH. Recent progress in biomedical applications of titanium dioxide. *Phys Chem Chem Phys*. 2013;15(14):4844-4858.
18. Saleh NB, Milliron DJ, Aich N, Katz LE, Liljestrand HM, Kirisits MJ. Importance of doping, dopant distribution, and defects on electronic band structure alteration of metal oxide nanoparticles: implications for reactive oxygen species. *Sci Total Environ*. 2016;568:926-932.
19. Xia T, Zhao Y, Sager T, et al. Decreased dissolution of ZnO by iron doping yields nanoparticles with reduced toxicity in the rodent lung and zebrafish embryos. *ACS Nano*. 2011;5(2):1223-1235.
20. Li M, Pokhrel S, Jin X, Mädler L, Damoiseaux R, Hoek EM. Stability, bioavailability, and bacterial toxicity of ZnO and iron-doped ZnO nanoparticles in aquatic media. *Environ Sci Technol*. 2010;45(2):755-761.
21. George S, Pokhrel S, Ji Z, et al. Role of Fe doping in tuning the band gap of TiO_2 for the photo-oxidation-induced cytotoxicity paradigm. *J Am Chem Soc*. 2011;133(29):11270-11278.
22. Rimai L, Heyde ME, Carew EB. Effect of divalent metal ion binding on the Raman spectrum of ATP in aqueous solution. *Biochem Biophys Res Commun*. 1970;38(2):231-237.
23. Rimai L, Heyde ME. An investigation by Raman spectroscopy of the base-proton dissociation of ATP in aqueous solution and the interactions of ATP with Zn^{++} and Mn^{++}. *Biochem Biophys Res Commun*. 1970;41(2):313-320.

24. Zhelyaskov V, Yue KT. A Raman study of the binding of Fe(III) to ATP and AMP. *Biochem J*. 1992;287(2):561-566.
25. Bhaumik A, Shearin AM, Delong R, Wanekaya A, Ghosh K. Probing the interaction at the nano-bio interface using Raman spectroscopy: ZnO nanoparticles and adenosine triphosphate biomolecules. *J Phys Chem C*. 2014;118(32):18631-18639.
26. Luu CL, Nguyen QT, Ho ST. Synthesis and characterization of Fe-doped TiO_2 photocatalyst by the sol-gel method. *Adv Nat Sci Nanosci Nanotechnol*. 2010;1(1):015008.
27. Yang Y, Yu Y, Wang J, Zheng W, Cao Y. Doping and transformation mechanisms of Fe^{3+} ions in Fe-doped TiO_2. *CrstEngComm*. 2017;19(7):1100-1105.
28. Othman SH, Rashid SA, Ghazi TM, Abdullah N. Effect of Fe doping on phase transition of TiO_2 nanoparticles synthesized by MOCVD. *J Appl Sci*. 2010;10(12):1044-1051.
29. Mathews NR, Jacome MC, Angeles-Chavez C, Antonio JT. Fe doped TiO_2 powder synthesized by sol gel method: structural and photocatalytic characterization. *J Mater Sci Mater Electron*. 2015;26(8):5574-5584.
30. Richter H, Wang ZP, Ley L. The one phonon Raman spectrum in microcrystalline silicon. *Solid State Commun*. 1981;39(5):625-629.
31. Rajalakshmi M, Arora AK, Bendre BS, Mahamuni S. Optical phonon confinement in zinc oxide nanoparticles. *J Appl Phys*. 2000;87(5):2445-2448.
32. Sekiya T, Ohta S, Kamei S, Hanakawa M, Kurita S. Raman spectroscopy and phase transition of anatase TiO_2 under high pressure. *J Phys Chem Solid*. 2001;62(4):717-721.
33. Chen L, Yang X, Chen J, et al. Continuous shape- and spectroscopy-tuning of hematite nanocrystals. *Inorg Chem*. 2010;49(18):8411-8420.
34. Rimai L, Cole T, Parsons JL, Hickmott JT Jr, Carew EB. Studies of Raman spectra of water solutions of adenosine tri-, di-, and monophosphate and some related compounds. *Biophys J*. 1969;9(3):320-329.
35. McCusker LB, Von Dreele RB, Cox DE, Louër D, Scardi P. Rietveld refinement guidelines. *J Appl Cryst*. 1999;32(1):36-50.
36. Bonvin D, Bastiaansen JA, Stuber M, Hofmann H, Ebersold MM. ATP and NADPH coated iron oxide nanoparticles for targeting of highly metabolic tumor cells. *J Mater Chem B*. 2017;5(42):8353-8365.
37. Cohn M, Hughes TR. Nuclear magnetic resonance spectra of adenosine di- and triphosphate II. Effect of complexing with divalent metal ions. *J Biol Chem*. 1962;237(1):176-181.
38. Hofmann KP, Zundel G. Stepwise protonation of PO_4^{3-}, ADP and ATP salts, IR investigations. *Z Naturforsch C*. 1974;29(1–2):19-28.
39. Uetsuki K, Verma P, Yano TA, Saito Y, Ichimura T, Kawata S. Experimental identification of chemical effects in surface enhanced Raman scattering of 4-aminothiophenol. *J Phys Chem C*. 2010;114(16):7515-7520.
40. Szabó Z. Multinuclear NMR studies of the interaction of metal ions with adenine-nucleotides. *Coord Chem Rev*. 2008;252(21–22):2362-2380.
41. Singh SK, Das A. The n→π* interaction: a rapidly emerging non-covalent interaction. *Phys Chem Chem Phys*. 2015;17(15):9596-9612.
42. Zhang M, Zhou N, Yuan P, Su Y, Shao M, Chi C. Graphene oxide and adenosine triphosphate as a source for functionalized carbon dots with applications in pH-triggered drug delivery and cell imaging. *RSC Adv*. 2017;7(15):9284-9293.

How to cite this article: Barkhade T, Phatangare A, Dahiwale S, Mahapatra SK, Banerjee I. Nano-bio interface study between Fe content TiO_2 nanoparticles and adenosine triphosphate biomolecules. *Surf Interface Anal*. 2019;51:894–905. https://doi.org/10.1002/sia.6663